GEOPHYSICS, VOL. 72, NO. 5 (SEPTEMBER-OCTOBER 2007); P. SM35–SM46, 10 FIGS., 1 TABLE.
10.1190/1.2750639

Generalization of von Neumann analysis for a model of two discrete half-spaces: The acoustic case

Matthew M. Haney[1]

ABSTRACT

Evaluating the performance of finite-difference algorithms typically uses a technique known as von Neumann analysis. For a given algorithm, application of the technique yields both a dispersion relation valid for the discrete time-space grid and a mathematical condition for stability. In practice, a major shortcoming of conventional von Neumann analysis is that it can be applied only to an idealized numerical model — that of an infinite, homogeneous whole space. Experience has shown that numerical instabilities often arise in finite-difference simulations of wave propagation at interfaces with strong material contrasts. These interface instabilities occur even though the conventional von Neumann stability criterion may be satisfied at each point of the numerical model. To address this issue, I generalize von Neumann analysis for a model of two half-spaces. I perform the analysis for the case of acoustic wave propagation using a standard staggered-grid finite-difference numerical scheme. By deriving expressions for the discrete reflection and transmission coefficients, I study under what conditions the discrete reflection and transmission coefficients become unbounded. I find that instabilities encountered in numerical modeling near interfaces with strong material contrasts are linked to these cases and develop a modified stability criterion that takes into account the resulting instabilities. I test and verify the stability criterion by executing a finite-difference algorithm under conditions predicted to be stable and unstable.

INTRODUCTION

The finite-difference method has progressed a long way since the pioneering efforts of Fermi, Pasta, and Ulam (Fermi et al., 1955). Today, moderately sized ($\sim 10^7$ gridpoints) finite-difference simulations of the 3D acoustic wave equation may be executed in a single workstation computational environment. Simulations of large-scale numerical models are planned (e.g., Bednar et al., 2006), and the benefit of accurate full-waveform seismic modeling by finite differences is by now well established (Kelly and Marfurt, 1990). However, even with access to the requisite computing power and code capable of faithfully simulating 3D wave propagation, a complete understanding of numerical algorithm performance is necessary to put the tool to best use.

The evaluation of algorithm performance has attracted the attention of many researchers. The most widely considered aspects of algorithm performance have tended to be numerical dispersion (both phase and group) and stability (Alterman and Lowenthal, 1970; Levander, 1988; Lines et al., 1999; Moczo et al., 2000; Hestholm, 2003). Some attention has been devoted to less well-known aspects, such as numerical polarization error (Marfurt, 1984). The concepts of numerical dispersion and stability also apply to finite-element (Marfurt, 1984) and spectral-element codes (Komatitsch and Tromp, 1999), although in this work I limit the discussion to finite-difference algorithms.

Stability and dispersion of a numerical algorithm (e.g., a finite-difference or finite-element code) are closely related topics. Three techniques exist to establish numerical stability (Haltiner and Williams, 1980): the matrix method, von Neumann analysis (named for the famous Hungarian mathematician, John von Neumann), and the energy method (Cohen, 2001). Of these techniques, the matrix method and von Neumann analysis are similar conceptually. In fact, it can be said that von Neumann analysis is equivalent to the matrix method for a model of an infinite, homogeneous whole space. The matrix method represents a numerically calculated quantity $\mathbf{u}$ at time index $n + 1$ as a matrix $\mathbf{A}$ multiplied by the same quantity at the previous time index n:

$$\mathbf{u}_{n+1} = \mathbf{A}\mathbf{u}_n. \tag{1}$$

The matrix $\mathbf{A}$ is called the amplification matrix. In principle, the matrix method is quite simple. For stability with respect to exponential growth, it studies the eigenvalues of $\mathbf{A}$, and stability is established if

Manuscript received by the Editor December 5, 2006; revised manuscript received March 10, 2007; published online August 23, 2007; corrected version published online August 28, 2007.
[1]Formerly Sandia National Laboratories, Geophysics Department, Albuquerque, New Mexico; presently USGS Alaska Volcano Observatory, Anchorage, Alaska. E-mail: mhaney@usgs.gov.

all eigenvalues have magnitudes less than or equal to unity (Haltiner and Williams, 1980). Numerical dispersion can in turn be studied by looking at the eigenvectors of **A** (Scales, 1995). The generality of the matrix method, evident from the form of equation 1, means that heterogeneous models and discrete boundary conditions can be treated. The matrix method has been applied in exploration seismics to estimate the stability of explicit depth extrapolators (Wapenaar et al., 1995).

Despite its simplicity and generality, the matrix method suffers as an analytical tool because only a limited number of matrices have closed-form expressions for their eigenvalues and eigenvectors. The tridiagonal matrix is a notable exception (Scales, 1995; p. 193). Thus, application of the matrix method in practice relies on the ability to find the eigenvalues and eigenvectors of a large, sparse matrix numerically (Koteras and Lehoucq, 2007). Besides not providing simple, analytical insight into the stability condition, the computational demands of such an approach may in fact rival the demands of executing a finite-difference code itself. Thus, although von Neumann analysis is less general than the matrix method, it does allow a concise, quantitative understanding of the properties of numerical algorithms.

There is, however, one severe limitation to von Neumann analysis in practice: It can only be applied to an idealized model of an infinite, homogeneous whole space. Several texts on numerical algorithms have hinted at this limitation of conventional von Neumann analysis. For example, in the literature it has been stated that,

- "… [the von Neumann method] is sufficient for linear equations with constant coefficients since separate solutions are additive" (Haltiner and Williams, 1980).
- "… von Neumann analysis is local: We imagine that the coefficients of the difference equations are so slowly varying as to be considered constant in space and time" (Press et al., 1986).
- "… [von Neumann] analysis is applicable to linear FDE with constant coefficients" (Moczo et al., 2004).

Based on these statements, it is logical to expect that von Neumann analysis should encounter difficulties for heterogeneous models.

Before going further, I illustrate the limitations of von Neumann analysis with an example. For this example, I numerically simulate acoustic waves propagating in a model of two half-spaces using a finite-difference code developed within the Geophysics Department at Sandia National Laboratories. Here and elsewhere in this paper, I use a model in which there only exists a contrast in density between the two half-spaces. In Table 1, seven such models are described in terms of their relevant parameters. Here, I use model 2. Figure 1, shows time slices of the numerically simulated pressure wavefield for an explosion source situated in medium 1. Note that the simulations are three dimensional; the plot in Figure 1 is a single vertical plane from the full 3D wavefield. The simulated pressure wavefield in Figure 1 propagates outward from the source position and eventually interacts with the interface between the two media. Reflected and transmitted waves arise at the interface. The interface is a pure density contrast, so there is no ray bending, and the transmitted wavefield in medium 2 maintains the property of being a spherically diverging wave. Note that periodic boundary conditions are imposed at the vertical sides of the model. These boundary conditions produce the apparent reflections from the sides of the model in the time slice of Figure 1 taken at $t = 0.08$ s.

Table 1. Models 1–7 contain a pure density contrast and differ only in the value of density in the transmitting medium, denoted medium 2. Grid spacing and time step are also given for the examples in the text.

Medium	Model	ρ (kg/m^3)	c (m/s)	Δt (s)	h (m)
1	1–7	2200	2500	0.00025	1.5
2	1	500	2500	0.00025	1.5
	2	100	2500	0.00025	1.5
	3	80	2500	0.00025	1.5
	4	60	2500	0.00025	1.5
	5	50	2500	0.00025	1.5
	6	40	2500	0.00025	1.5
	7	30	2500	0.00025	1.5

The simulation in Figure 1 executes in a stable fashion, meaning that no exponentially growing amplitudes emerge in the modeled wavefield. This property in not unexpected; as discussed in a later section of this paper, the von Neumann stability criterion for the finite-difference algorithm used here is

$$c\Delta t \leq \frac{h}{\sqrt{3}}, \tag{2}$$

where c is the wave speed, Δt is the time step, and h is the grid spacing (the same in all three coordinate directions). For the model used in Figure 1 (model 2), the parameters given in Table 1 satisfy the stability criterion in both the upper and lower half-spaces. Thus, it is not surprising that the simulation is numerically stable.

The stability criterion given by equation 2 does not depend on density. Therefore, one would expect that changing the density values for the model shown in Figure 1 should have no bearing on whether the simulation executes stably or not. This idea is tested in Figure 2. In this figure, a comparison is made between the previous simulation, which uses model 2, and a simulation using model 3. As shown in Table 1, model 3 is identical to model 2 except that the density of one of the half-spaces (medium 2) is slightly lower. Figure 2a depicts two time slices for the simulation with model 2 (repeated from Figure 1, for comparison), and Figure 2b depicts two time slices for model 3. In clear contradiction to the notion that density has no impact on numerical stability, a strong instability is seen to arise at the interface for model 3. This instability is absent for the simulation using model 2. From Figure 2b, it appears that the instability arises in the simulation before the incident wavefield from the explosive source arrives at the interface. In fact, the instability begins when a small amount of the wavefield, ahead of the main portion of the source waveform (a Ricker wavelet), arrives at the interface. As is the case generally for numerical instabilities, the initially small incident wavefield rapidly turns into an artificial (i.e., nonphysical), high-amplitude waveform. The high amplitude eventually causes the numerical simulation to terminate prematurely as a result of floating-point overflow. This type of instability apparently is caused by the stronger density contrast across the interface for model 3 compared to model 2.

The aim of this paper is to address such interface stability problems by generalizing conventional von Neumann analysis to allow

for a heterogeneous model. In this paper, I use the simplest example of a heterogeneous model — that of two half-spaces. I embark on this investigation bearing in mind the documented occurrences of numerical instabilities at interfaces with strong material contrasts (Crase, 1990; Seron et al., 1996; Bartel et al., 2000; Saenger et al., 2000). These instabilities arise even though the stability criterion derived using conventional von Neumann analysis may be satisfied for each gridpoint in the numerical model. A generalized von Neumann approach for a model of two discrete half-spaces should provide insight into the origin of this type of interface instability. In addition, it should provide a quantitative means to analyze the accuracy of discrete reflection and transmission coefficients.

The organization of the paper is as follows. I begin by reviewing the conventional von Neumann approach for an $O(2,2)$ heterogeneous acoustic standard staggered-grid scheme, where $O(2,2)$ represents second-order accuracy in time and second-order accuracy in space. Then the same scheme is described for a model with depth variation only. I continue by deriving closed-form expressions for reflection and transmission coefficients that account for the discrete time-space grids. These expressions for discrete reflection and transmission coefficients are used to study instabilities in a half-space model and derive a stability criterion that accounts for these instabilities. To test this new stability criterion, a finite-difference code is executed for waves normally-incident on a discrete interface between two half-spaces. The new stability criterion in the case of general 3D wave propagation is tested by re-examining the example described above. Finally, a discussion of the extension of our generalized von Neumann approach to higher-order accurate spatial schemes, such as $O(2,4)$ is presented.

CONVENTIONAL VON NEUMANN ANALYSIS FOR A STANDARD STAGGERED-GRID SCHEME

Consider acoustic wave propagation as described by the velocity-pressure system of equations in the absence of sources:

$$\rho\frac{\partial v^x}{\partial t} + \frac{\partial p}{\partial x} = 0, \tag{3}$$

$$\rho\frac{\partial v^y}{\partial t} + \frac{\partial p}{\partial y} = 0, \tag{4}$$

$$\rho\frac{\partial v^z}{\partial t} + \frac{\partial p}{\partial z} = 0, \tag{5}$$

$$\frac{\partial p}{\partial t} + \kappa\left(\frac{\partial v^x}{\partial x} + \frac{\partial v^y}{\partial y} + \frac{\partial v^z}{\partial z}\right) = 0. \tag{6}$$

In equations 3–6, v^x, v^y, and v^z are the particle velocities in the three Cartesian coordinate directions (x, y, and z), p is the pressure, $\rho = \rho(x,y,z)$ is the density of the medium, and $\kappa = \kappa(x,y,z)$ is the bulk modulus. Staggered-grid, finite-difference methods find the solution of a discrete version of equations 3–6. In this paper, I use a numerical scheme that is second-order accurate in time and second-order accurate in space, called $O(2,2)$ in shorthand notation. It is also a heterogeneous scheme, meaning that material property variation is accounted for implicitly without enforcing explicit boundary conditions in the algorithm (Kelly et al., 1976; Zahradník and Priolo, 1995). The velocity-pressure system of equations is well suited for this approach because no spatial derivatives of material properties exist. Furthermore, codes based on such heterogeneous schemes do not require the user to set boundary conditions interactively at every internal interface of the model, thus making the requirements for the user less demanding. The $O(2,2)$ heterogeneous finite-difference stencil for the velocity-pressure system of equations, shown in equations 3–6, is

$$v^x_{l+1/2,q,m,n+1/2} = v^x_{l+1/2,q,m,n-1/2} - \frac{\Delta t}{h_x \rho_{l+1/2,q,m}} \times (p_{l+1,q,m,n} - p_{l,q,m,n}), \tag{7}$$

$$v^y_{l,q+1/2,m,n+1/2} = v^y_{l,q+1/2,m,n-1/2} - \frac{\Delta t}{h_y \rho_{l,q+1/2,m}} \times (p_{l,q+1,m,n} - p_{l,q,m,n}), \tag{8}$$

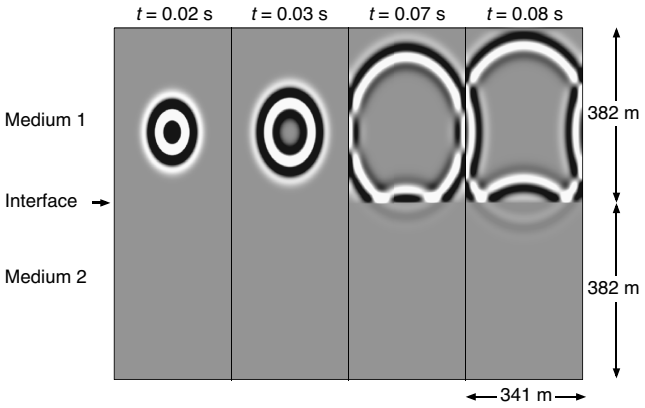

Figure 1. Four time-slice plots showing the diverging pressure wavefield for a model of two half-spaces caused by an explosive source in the upper medium, medium 1. The model used for this simulation is model 2, described in Table 1. As predicted by von Neumann analysis, the simulation executes in a stable manner.

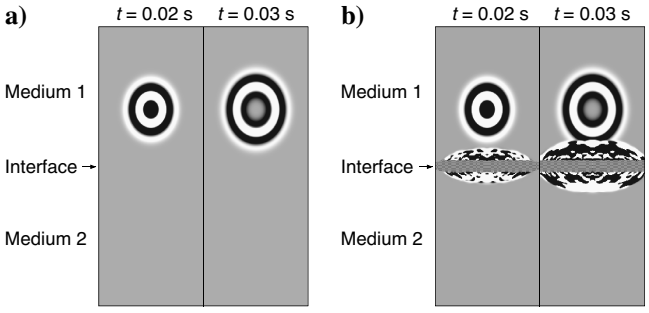

Figure 2. Two time-slice plots each for two different models: (a) model 2 and (b) model 3. As described in Table 1, model 3 has a slightly larger density contrast across the interface than does model 2. The two time slice plots in (a) are identical to the first two time slice plots depicted in Figure 1. A strong instability occurs at the interface in (b) for the simulation using model 3. Such an instability is not predicted based on conventional von Neumann analysis. Thus, the instability is evidence of the limitations of the method.

$$v^z_{l,q,m+1/2,n+1/2} = v^z_{l,q,m+1/2,n-1/2} - \frac{\Delta t}{h_z \rho_{l,q,m+1/2}} \times (p_{l,q,m+1,n} - p_{l,q,m,n}), \quad (9)$$

$$p_{l,q,m,n+1} = p_{l,q,m,n} - \frac{\kappa_{l,q,m}\Delta t}{h_x} \times (v^x_{l+1/2,q,m,n+1/2} - v^x_{l-1/2,q,m,n+1/2}) - \frac{\kappa_{l,q,m}\Delta t}{h_y}(v^y_{l,q+1/2,m,n+1/2} - v^y_{l,q-1/2,m,n+1/2}) - \frac{\kappa_{l,q,m}\Delta t}{h_z}(v^z_{l,q,m+1/2,n+1/2} - v^z_{l,q,m-1/2,n+1/2}). \quad (10)$$

In equations 7–10, the indices l, q, and m refer to the x-, y-, and z-coordinates in discrete space; the index n refers to the discrete time coordinate; h_x, h_y, and h_z are the grid spacings; and Δt is the time step. The location of the various quantities within the standard staggered grid is shown in Figure 3. The standard staggered-grid indexing scheme originates from the work of Virieux (1984, 1986). In this paper, I consider a grid equally spaced in each direction for simplicity: $h_x = h_y = h_z = h$.

The first step in conventional von Neumann analysis is to transform equations 7–10 from discrete time and space to continuous frequency and wavenumber using the discrete-time Fourier transform (DTFT) and discrete-space Fourier transform (DSFT). Such transformations are only advantageous if the model is shift invariant in the respective time and space coordinates, i.e., an infinite homogeneous whole space. The DTFT and DSFT are related directly to the z-transform encountered in signal processing (Claerbout, 1976). They should not be confused with the discrete Fourier transform

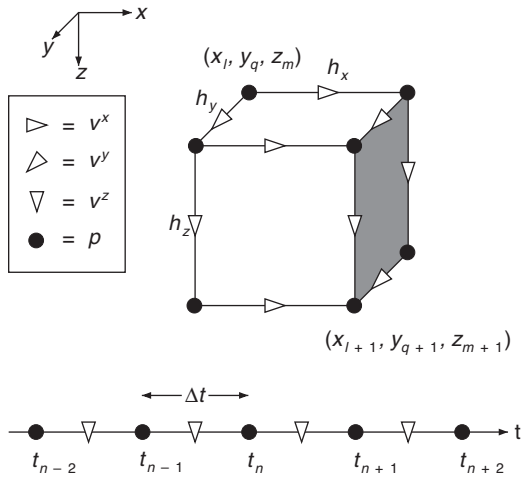

Figure 3. Unit cell for a velocity-pressure finite-difference scheme on a standard staggered grid. Material properties ρ and κ are stored on the integer raster, coincident with pressure. Although only v^z is shown as being updated at the half-integer time step, all velocities are updated simultaneously. Adapted from Aldridge et al. (2004).

(DFT), which maps discrete time or space to discrete frequency or wavenumber (Oppenheim and Willsky, 1983). Given a general discrete time series u_m, with an index m taking values from $-\infty$ to ∞, the convention used for the forward DTFT in this paper is

$$U(\omega\Delta t) = \sum_{m=-\infty}^{\infty} u_m \exp(-i\omega\Delta t m), \quad (11)$$

where ω is frequency and Δt is the sampling rate in time. Accordingly, the inverse DTFT is

$$u_m = \frac{1}{2\pi}\int_{-\pi}^{\pi} U(\omega\Delta t)\exp(i\omega\Delta t m)d(\omega\Delta t). \quad (12)$$

Note that the dual variable of the index m is dimensionless frequency $\omega\Delta t$. In what follows, extensive use is made of the shift theorem for the DTFT,

$$u_{m+q} \leftrightarrow U(\omega\Delta t)\exp(i\omega\Delta t q), \quad (13)$$

where the symbol $\leftrightarrow$ shows the relationship between dual quantities and q is a discrete shift. The DSFT is defined identically to the DTFT for a discrete spatial series.

For an infinite homogeneous whole space, conventional von Neumann analysis proceeds by taking the DTFT and three DSFTs over the four indices l, q, m, and n. I refer to wavefield quantities transformed over l, q, m, and n as fully transformed. Denoting the fully transformed pressure and velocities with capital letters V^x, V^y, V^z, and P, the application of the DTFT and DSFT to equations 7–10 results in

$$V^x \exp\left(\frac{ik_x h}{2}\right)\left[\exp\left(\frac{i\omega\Delta t}{2}\right) - \exp\left(\frac{-i\omega\Delta t}{2}\right)\right] = -\frac{\Delta t}{h\rho}P[\exp(ik_x h) - 1], \quad (14)$$

$$V^y \exp\left(\frac{ik_y h}{2}\right)\left[\exp\left(\frac{i\omega\Delta t}{2}\right) - \exp\left(\frac{-i\omega\Delta t}{2}\right)\right] = -\frac{\Delta t}{h\rho}P[\exp(ik_y h) - 1], \quad (15)$$

$$V^z \exp\left(\frac{ik_z h}{2}\right)\left[\exp\left(\frac{i\omega\Delta t}{2}\right) - \exp\left(\frac{-i\omega\Delta t}{2}\right)\right] = -\frac{\Delta t}{h\rho}P[\exp(ik_z h) - 1], \quad (16)$$

$$P[\exp(i\omega\Delta t) - 1] = -\frac{\kappa\Delta t}{h}V^x \exp\left(\frac{i\omega\Delta t}{2}\right)\left[\exp\left(\frac{ik_x h}{2}\right) - \exp\left(\frac{-ik_x h}{2}\right)\right] - \frac{\kappa\Delta t}{h}V^y \exp\left(\frac{i\omega\Delta t}{2}\right)\left[\exp\left(\frac{ik_y h}{2}\right) - \exp\left(\frac{-ik_y h}{2}\right)\right] - \frac{\kappa\Delta t}{h}V^z \exp\left(\frac{i\omega\Delta t}{2}\right)\left[\exp\left(\frac{ik_z h}{2}\right) - \exp\left(\frac{-ik_z h}{2}\right)\right]. \quad (17)$$

Using equations 14–16 to substitute for V^x, V^y, and V^z in equation 17 provides a single equation in terms of the fully transformed pressure:

$$P\left[(\cos\omega\Delta t - 1) + \frac{2\kappa\Delta t^2}{\rho h^2}\left(\sin^2\frac{k_x h}{2} + \sin^2\frac{k_y h}{2} + \sin^2\frac{k_z h}{2}\right)\right] = 0. \quad (18)$$

In equation 18, the quantity in brackets is the discrete dispersion relation; it relates ω, k_x, k_y, and k_z for nontrivial solutions. Using half-angle identities and denoting the wavespeed $c^2 = \kappa/\rho$, the dispersion relation is

$$\omega\Delta t = \pm\arccos\left[1 + \frac{c^2\Delta t^2}{h^2}[\cos(k_x h) + \cos(k_y h) + \cos(k_z h) - 3]\right]. \quad (19)$$

When the sampling in space and time is dense, $k_x h$, $k_y h$, $k_z h$, and $\omega\Delta t$ are small quantities ($\ll 1$). In the continuum limit, only the highest-order term for these quantities needs to be retained (Scales, 1995). Thus, an expansion of the terms in equation 19 to second order in $k_x h$, $k_y h$, $k_z h$, and $\omega\Delta t$ gives the usual dispersion relation for a continuum:

$$\omega^2 = c^2(k_x^2 + k_y^2 + k_z^2). \quad (20)$$

Stability considerations require the argument of the inverse cosine function in equation 19 to be less than or equal to one and greater than or equal to -1. Examining equation 19, the argument of the inverse cosine is seen to be always less than or equal to one (Lines et al., 1999). Thus, stability only relies on the argument being greater than or equal to -1 for all possible k_x, k_y, and k_z. It turns out that the most stringent condition occurs when $k_x h = k_y h = k_z h = \pi$. There, the condition states that $1 - 6c^2\Delta t^2/h^2 \geq -1$, or, in other words,

$$c\Delta t \leq \frac{h}{\sqrt{3}}. \quad (21)$$

This is the stability condition for the $O(2,2)$ scheme on a grid equally spaced in all directions, $h_x = h_y = h_z = h$. It is the stability criterion discussed in the introduction and given by equation 2.

To see why the argument of the inverse cosine being less than -1 causes an instability, note that $\arccos(-1 - \delta) = \pi - i\epsilon$, where δ and ϵ are related positive numbers. From equation 19, two solutions for $\omega\Delta t$ exist that are equal in magnitude but opposite in sign: $\omega\Delta t = \pm(\pi - i\epsilon)$. Thus, one of the two solutions will grow exponentially in time and the other will decay exponentially in time. The growing solution is the culprit behind numerical instability. From the convention for the DTFT in equation 12, I can identify which of the two solutions is the growing, unstable solution: $\omega\Delta t = \pi - i\epsilon$.

It is useful to express the vertical wavenumber in terms of k_x, k_y, and ω for the $O(2,2)$ scheme:

$$k_z h = \pm\arccos\left[1 + \frac{h^2}{c^2\Delta t^2}(\cos\omega\Delta t - 1) + 2 - \cos k_x h - \cos k_y h\right]. \quad (22)$$

Two values of k_z satisfy the dispersion relation for a particular k_x, k_y, and ω. These two solutions can be seen as an up- and a downgoing wave. This expression proves to be useful when considering reflection and transmission coefficients of waves for a model of two discrete half-spaces, as discussed in a following section.

STANDARD STAGGERED GRID FOR A MODEL WITH DEPTH VARIATION

Consider a model whose material parameters depend on the vertical index m. This model is not shift invariant in the vertical direction, and I hold off on taking a DSFT over this dimension. The pressure and velocities transformed over only the horizontal indices and the time index therefore retain a dependence on the vertical index m. Denoting with capital letters and the subscript m these partially transformed quantities as V^x_m, V^y_m, V^z_m, and P_m, the application of the DTFT and two DSFTs to equations 7–10 results in

$$V^x_m \exp\left(\frac{ik_x h}{2}\right)\left[\exp\left(\frac{i\omega\Delta t}{2}\right) - \exp\left(\frac{-i\omega\Delta t}{2}\right)\right] = -\frac{\Delta t}{h\rho_m}P_m[\exp(ik_x h) - 1], \quad (23)$$

$$V^y_m \exp\left(\frac{ik_y h}{2}\right)\left[\exp\left(\frac{i\omega\Delta t}{2}\right) - \exp\left(\frac{-i\omega\Delta t}{2}\right)\right] = -\frac{\Delta t}{h\rho_m}P_m[\exp(ik_y h) - 1], \quad (24)$$

$$V^z_{m+1/2}\left[\exp\left(\frac{i\omega\Delta t}{2}\right) - \exp\left(\frac{-i\omega\Delta t}{2}\right)\right] = -\frac{\Delta t}{h\rho_{m+1/2}}[P_{m+1} - P_m], \quad (25)$$

$$\begin{aligned} P_m[\exp(i\omega\Delta t) - 1] &= -\frac{\kappa_m\Delta t}{h}V^x_m \exp\left(\frac{i\omega\Delta t}{2}\right)\left[\exp\left(\frac{ik_x h}{2}\right) - \exp\left(\frac{-ik_x h}{2}\right)\right] \\ &\quad - \frac{\kappa_m\Delta t}{h}V^y_m \exp\left(\frac{i\omega\Delta t}{2}\right) \\ &\quad \times\left[\exp\left(\frac{ik_y h}{2}\right) - \exp\left(\frac{-ik_y h}{2}\right)\right] - \frac{\kappa_m\Delta t}{h}\exp\left(\frac{i\omega\Delta t}{2}\right) \\ &\quad \times[V^z_{m+1/2} - V^z_{m-1/2}]. \end{aligned} \quad (26)$$

As in the case of an infinite homogeneous whole space, I use equations 23–25 to substitute for V^x_m, V^y_m, $V^z_{m+1/2}$, and $V^z_{m-1/2}$ in equation 26. I thus arrive at a single equation in terms of the partially transformed pressure:

$$2(\cos\omega\Delta t - 1)\frac{h^2}{\kappa_m\Delta t^2}P_m = \frac{P_{m+1}}{\rho_{m+1/2}} - \left[\frac{1}{\rho_{m+1/2}} + \frac{1}{\rho_{m-1/2}} + \frac{2(2 - \cos k_x h - \cos k_y h)}{\rho_m}\right]P_m + \frac{P_{m-1}}{\rho_{m-1/2}}. \quad (27)$$

This expression relates the partially transformed pressure P_m at three consecutive gridpoints, $m - 1$, m, and $m + 1$. In the case of an infinite homogeneous whole space, it simplifies into equation 18 after a DSFT over the index m.

In the standard staggered-grid system of equations, the velocity and pressure are stored on grids staggered in both discrete space and time, as shown in Figure 3. However, the model parameters ρ and κ exist only on the integer values of l, q, and m (see Figure 3). Equation 27 requires the density at the indices $m + 1/2$ and $m - 1/2$, so an averaging rule must be used to relate $\rho_{m+1/2}$ and $\rho_{m-1/2}$ to the values on the integer raster. The averaging rule adopted in this paper takes the average of the reciprocals of the two nearby densities:

$$\frac{1}{\rho_{m+1/2}} = \frac{1}{2}\left(\frac{1}{\rho_m} + \frac{1}{\rho_{m+1}}\right). \quad (28)$$

Other averaging rules for density have been suggested in the literature (Moczo et al., 2002). Although I do not investigate other averaging rules in this paper, the generalized von Neumann analysis described in the following sections can be used with other types of averaging. Given the above rule, equation 27 becomes

$$2(\cos\omega\Delta t - 1)\frac{h^2}{\kappa_m\Delta t^2}P_m = \frac{P_{m+1}}{2}\left[\frac{1}{\rho_m} + \frac{1}{\rho_{m+1}}\right] - \left[\frac{1}{2\rho_{m+1}} + \frac{1}{2\rho_{m-1}} + \frac{1 + 2(2 - \cos k_x h - \cos k_y h)}{\rho_m}\right]P_m + \frac{P_{m-1}}{2}\left[\frac{1}{\rho_{m-1}} + \frac{1}{\rho_m}\right]. \quad (29)$$

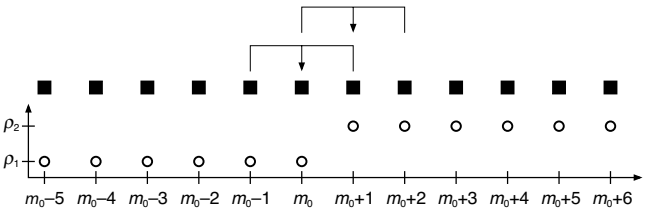

Figure 4. A scheme that is second order in space. There are two wave modes in this case (an upgoing and a downgoing wave); thus, only two relationships are needed to solve for the one reflected wave and one transmitted wave from the discrete interface. These two relationships are analogous to boundary conditions in the continuum case and are given by the two finite-difference stencils which overlap between the two half-spaces.

This equation represents the partially transformed finite-difference stencil for pressure for a discrete model, which generally varies in the vertical index m. It can be used to examine the particular case of two discrete half-spaces.

REFLECTION AND TRANSMISSION FOR A MODEL OF TWO DISCRETE HALF-SPACES

To find a stability condition for a model of two half-spaces, one must first find the expressions for the reflection and transmission coefficients accounting for the discrete time and space grids. The approach here is a generalization of the usual calculation for reflection and transmission coefficients at an interface: The wavefield on either side of the interface consists of incident, reflected, and transmitted waves, and boundary conditions provide enough relationships to uniquely determine the reflection and transmission coefficients.

An important distinction between the current case of discrete time-space grids and the usual calculation in a continuum is that boundary conditions are not explicitly given for a heterogeneous finite-difference scheme. Even if they were, the notion of a sharp boundary does not even exist in the discrete case; all that exists is a jump in material properties between two adjoining gridpoints of a model (see Figure 4). What is needed for the calculation of discrete reflection and transmission coefficients are two relationships that couple the wavefield in one of the half-spaces to the wavefield in the other half-space. These two relationships are in fact given by equation 29 for the two instances when the overlap of the finite-difference stencil lies in both half-spaces, as shown in Figure 4.

Consider, as in Figure 4, that the jump in material properties occurs between $m = m_0$ and $m = m_0 + 1$. Thus,

$$\rho_m = \rho_1 \quad \kappa_m = \kappa_1 \quad \text{for } m \le m_0,$$
$$\rho_m = \rho_2 \quad \kappa_m = \kappa_2 \quad \text{for } m > m_0. \quad (30)$$

For this model of two discrete half-spaces, assume the pressure wavefield comprises incident, reflected, and transmitted waves as

$$P_m = \exp(-ik_{z1}hm) + R\exp(ik_{z1}hm) \quad \text{for } m \le m_0,$$
$$P_m = T\exp(-ik_{z2}hm) \quad \text{for } m > m_0, \quad (31)$$

where k_{z1} and k_{z2} are the vertical wavenumbers for the two half-spaces. Bear in mind that these wavenumbers are not given by the dispersion relation in the continuum limit, e.g., $k_{z1} = \omega\cos\theta_1/c_1$, where θ_1 is the propagation angle and $c_1 = \sqrt{\kappa_1/\rho_1}$. The wavenumbers are given by equation 22, the discrete dispersion relation for the respective medium (1 or 2). Also, note that Snell's law holds for the discrete case, that is, $k_{x1} = k_{x2}$ and $k_{y1} = k_{y2}$.

Using equation 31, I proceed by evaluating equation 29 for the two cases $m = m_0$ and $m = m_0 + 1$. Without loss of generality, I set the index of the jump in material properties such that $m_0 = 0$. The choice of $m_0 = 0$ simplifies the discrete reflection and transmission coefficients in the same way as placing a horizontal interface at the origin of the depth axis simplifies the reflection and transmission coefficients for a continuum. The two cases yield two equations in terms of the (as yet unknown) reflection and transmission coefficients, R and T. Solving these equations for R and T gives expressions that take into account the discrete time-space grids for reflection and transmission:

$$R = \frac{A_{+}B - \frac{1}{4}\left(\frac{1}{\rho_1} + \frac{1}{\rho_2}\right)^2}{\frac{1}{4}\left(\frac{1}{\rho_1} + \frac{1}{\rho_2}\right)^2 - A_{-}B}, \tag{32}$$

$$T = \frac{\exp(ik_{z2}h)}{2B}\left(\frac{1}{\rho_1} + \frac{1}{\rho_2}\right) \times \frac{A_{+}B - A_{-}B}{\frac{1}{4}\left(\frac{1}{\rho_1} + \frac{1}{\rho_2}\right)^2 - A_{-}B}, \tag{33}$$

where

$$A_{\pm} = (\cos\omega\Delta t - 1)\frac{2h^2}{\kappa_1\Delta t^2} + \frac{1}{2}\left(\frac{3}{\rho_1} + \frac{1}{\rho_2}\right) + \frac{2(2 - \cos k_x h - \cos k_y h)}{\rho_1} - \frac{\exp(\pm ik_{z1}h)}{\rho_1},$$

$$B = (\cos\omega\Delta t - 1)\frac{2h^2}{\kappa_2\Delta t^2} + \frac{1}{2}\left(\frac{1}{\rho_1} + \frac{3}{\rho_2}\right) + \frac{2(2 - \cos k_x h - \cos k_y h)}{\rho_2} - \frac{\exp(-ik_{z2}h)}{\rho_2}. \tag{34}$$

In the continuum limit ($k_x h$, $k_y h$, $k_{z1}h$, $k_{z2}h$, and $\omega\Delta t \ll 1$), these discrete reflection and transmission coefficients give the usual expressions for acoustic reflection and transmission. I briefly demonstrate this for the reflection coefficient R.

To first order in $k_x h$, $k_y h$, $k_{z1}h$, $k_{z2}h$, and $\omega\Delta t$, the coefficients in equation 34 are

$$A_{\pm} \approx \frac{1}{2}\left(\frac{1}{\rho_1} + \frac{1}{\rho_2}\right) \mp \frac{ik_{z1}h}{\rho_1},$$
$$B \approx \frac{1}{2}\left(\frac{1}{\rho_1} + \frac{1}{\rho_2}\right) + \frac{ik_{z2}h}{\rho_2}. \tag{35}$$

Thus, to first order, the numerator of R is

$$A_{+}B - \frac{1}{4}\left(\frac{1}{\rho_1} + \frac{1}{\rho_2}\right)^2 \approx \frac{i}{2}\left(\frac{1}{\rho_1} + \frac{1}{\rho_2}\right)\left[\frac{k_{z2}h}{\rho_2} - \frac{k_{z1}h}{\rho_1}\right] \tag{36}$$

and the denominator is

$$\frac{1}{4}\left(\frac{1}{\rho_1} + \frac{1}{\rho_2}\right)^2 - A_{-}B \approx -\frac{i}{2}\left(\frac{1}{\rho_1} + \frac{1}{\rho_2}\right)\left[\frac{k_{z2}h}{\rho_2} + \frac{k_{z1}h}{\rho_1}\right]. \tag{37}$$

Taking the ratio of these quantities and noting that, in the continuum limit, $k_{z1} = \omega\cos\theta_1/c_1$ and $k_{z2} = \omega\cos\theta_2/c_2$, I find

$$R = \frac{\rho_2 c_2\cos\theta_1 - \rho_1 c_1\cos\theta_2}{\rho_2 c_2\cos\theta_1 + \rho_1 c_1\cos\theta_2}, \tag{38}$$

which is in agreement with the well-known reflection coefficient for pressure in acoustics (Tsvankin, 1995). The fact that the heterogeneous finite-difference equations implicitly model a welded interface (one with continuous particle velocity and pressure) agrees with findings of Zahradník and Priolo (1995).

Figure 5 shows the plot of the numerical reflection and transmission coefficients versus dimensionless frequency $\omega\Delta t$ at normal incidence. For the calculation, I use model 1 as described in Table 1. As $\omega\Delta t \to 0$, the numerical reflection and transmission coefficients converge to the exact values. However, as dimensionless frequency approaches Nyquist ($\omega\Delta t = \pi$), sampling is coarse and the numerical values deviate from the exact reflection and transmission coefficients. Note the sharp changes near $\omega\Delta t = \pm 1$. There, the incident wave becomes exponentially damped, in accordance with the dispersion relation of equation 22. This damping phenomenon does not occur in the continuum case, when $\omega = ck_z$ for normal incidence.

STABILITY AT A DISCRETE INTERFACE

For a model of two discrete half-spaces, three relevant criteria governing stability can be foreseen: (1) the usual stability condition (equation 21) in half-space 1, (2) the usual stability condition in half-space 2, and (3) a stability condition that accounts for instabilities generated at the interface. When unexpected instabilities arise at an interface of high material contrast, it must be that criteria 1 and 2 are satisfied, whereas criterion 3 is not. In this section, I investigate crite-

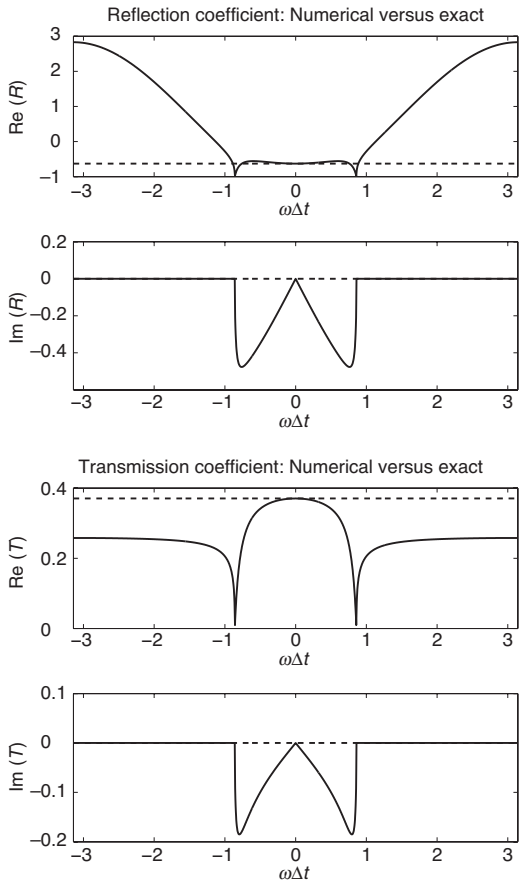

Figure 5. A comparison of numerical (solid line) and exact (dashed line) reflection and transmission coefficients in the case of normal incidence for model 1 as described in Table 1. The numerical reflection and transmission coefficients take into account the discrete time-space grids and converge to the exact (continuum) reflection and transmission coefficients as $\omega\Delta t \to 0$.

rion 3, assuming the first two criteria are satisfied. I therefore come to a stability condition that accounts for instabilities generated at interfaces.

Just as in the continuum limit, the discrete reflection and transmission coefficients (equations 32 and 33) have a common factor in their denominator. It is important to see if and when this denominator goes to zero. This situation is conceptually the same as the analysis for finding the occurrence of Rayleigh waves in the continuum elastic case because evanescent P- and S-waves can, by themselves, satisfy the boundary conditions at a stress-free surface between a solid and a vacuum (Lay and Wallace, 1995). With A_- and B given in equation 34, the behavior of the denominator D,

$$D = \frac{1}{4}\left(\frac{1}{\rho_1} + \frac{1}{\rho_2}\right)^2 - A_- B, \tag{39}$$

is studied to see if any instabilities satisfy $D = 0$ and under what conditions this occurs. The denominator in equation 39 is analogous to the famous Rayleigh determinant in the continuum elastic case. Waves that satisfy $D = 0$ (if they exist) are therefore akin to surface waves in the elastic case. In the continuum acoustic case, no such waves exist. However, I consider the acoustic case here for discrete media, so there is the chance that some nonphysical solutions exist that satisfy $D = 0$.

First, consider the stability of a wave normally incident on the discrete interface when k_x and $k_y = 0$. (Later, the most stringent case for stability in three dimensions is considered when $k_y h$ and $k_y h = \pi$.) As discussed for the case of a homogeneous whole space, an instability occurs when $\omega\Delta t = \pi - i\epsilon$ for $\epsilon > 0$. Thus, I substitute $k_x = 0$, $k_y = 0$, and $\omega\Delta t = \pi - i\epsilon$ into the expression for D. Then, I scan over $\epsilon > 0$ to see if any value of ϵ results in $D = 0$. If there exists such an ϵ, an instability is possible in the finite-difference solution. This procedure is analogous to the considerations outlined for an infinite homogeneous whole space. For clarification, if solutions of $D = 0$ exist that are stable ($\epsilon = 0$), then a nonphysical wave, similar to a surface wave, would emerge at the interface in the numerical simulations. Such a surface wave would not be desirable because it is nonphysical (i.e., not present in the continuum case), but at least it would not cause an instability. This case may in fact exist, although the likelihood of it occurring is rare compared to the unstable cases.

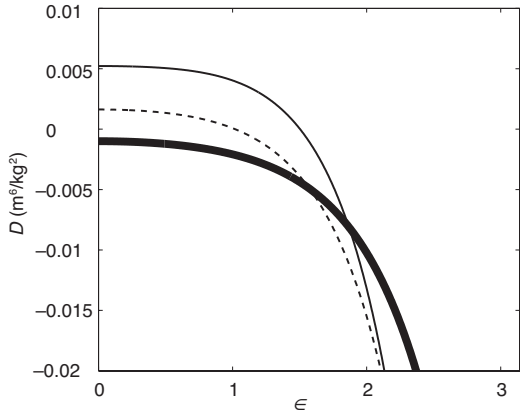

Figure 6. The denominator of the discrete reflection and transmission coefficients for different values of ϵ, the negative of the imaginary part of $\omega\Delta t$, for models 2 (thick solid line), 6 (thin dashed line), and 7 (thin solid line). The parameters for models 2, 6, and 7 are described in Table 1.

Shown in Figure 6 is the value of the denominator D versus ϵ for models 2 (thick solid line), 6 (thin dashed line), and 7 (thin solid line). Model descriptions are given in Table 1. Notice that for models 6 and 7, a zero crossing exists on the D versus ϵ plot. In contrast, model 2, which has a smaller density contrast, does not have a zero crossing. The presence of zero crossings for models 6 and 7 means their density contrast is large enough to generate an instability at the discrete interface. From continuity considerations, there must exist a single model with a density contrast between the ones given by models 2 and 6 that satisfies $D = 0$ for $\epsilon = 0$. In this rare case, a stable surface wave mode would emerge at the interface. I highlight this possibility to connect with the occurrence of surface waves, but I do not dwell on it because it only occurs for a single value of the density contrast. Instead, I am interested in the unstable wave modes that occur when the zero crossing happens for $\epsilon > 0$.

Figure 6 shows that, as ϵ increases, D becomes smaller and smaller, eventually becoming negative. Assuming that D is a continuous function of ϵ and is monotonically decreasing with increasing ϵ, an exact, though relatively uninformative, stability condition is

$$\lim_{\epsilon \to 0} D \leq 0. \tag{40}$$

Because D monotonically decreases with increasing ϵ, as shown in Figure 6, this condition ensures that D is not equal to zero for any ϵ. If D is never equal to zero for any ϵ, possible instabilities associated with the interface do not satisfy the conditions necessary for R and T to be unbounded. That is, the instabilities themselves do not satisfy the heterogeneous finite-difference equations and are not generated.

Although the stability condition (equation 40) is exact, it is preferable to write it in a more informative and concise form similar to the conventional von Neumann stability condition (equation 21). To do so demands that some approximations be made using the expression for D in equation 39 and the expressions for A_- and B given in equation 34. These approximations are tested in the following section. From equation 19, it turns out that, for $\epsilon \to 0$, the terms $\exp(-ik_{z1}h)$ and $\exp(-ik_{z2}h)$ can be approximated as

$$\exp(-ik_{z1}h) \approx -\frac{c_1^2\Delta t^2}{4h^2},$$
$$\exp(-ik_{z2}h) \approx -\frac{c_2^2\Delta t^2}{4h^2}. \tag{41}$$

These approximations are in error by terms that are fourth order and higher in $c_1\Delta t/h$ and $c_2\Delta t/h$, respectively. These expressions are useful because the terms $\exp(-ik_{z1}h)$ and $\exp(-ik_{z2}h)$ are present in equation 34 for A_- and B. With this approximation, the terms A_- and B can be expressed approximately as

$$A_- \approx \frac{1}{2}\left(\frac{3}{\rho_1} + \frac{1}{\rho_2}\right) - \frac{4h^2}{\kappa_1^2\Delta t^2} + \frac{1}{\rho_1}\frac{c_1^2\Delta t^2}{4h^2},$$
$$B \approx \frac{1}{2}\left(\frac{1}{\rho_1} + \frac{3}{\rho_2}\right) - \frac{4h^2}{\kappa_2^2\Delta t^2} + \frac{1}{\rho_2}\frac{c_2^2\Delta t^2}{4h^2}. \tag{42}$$

In both of these expressions, the third term on the right-hand side is much smaller than the second term. To see this, I can rewrite equation 42 as

$$A_- \approx \frac{1}{2}\left(\frac{3}{\rho_1}+\frac{1}{\rho_2}\right) - \frac{1}{\rho_1}\frac{4h^2}{c_1^2\Delta t^2} + \frac{1}{\rho_1}\frac{c_1^2\Delta t^2}{4h^2},$$
$$B \approx \frac{1}{2}\left(\frac{1}{\rho_1}+\frac{3}{\rho_2}\right) - \frac{1}{\rho_2}\frac{4h^2}{c_2^2\Delta t^2} + \frac{1}{\rho_2}\frac{c_2^2\Delta t^2}{4h^2}. \quad (43)$$

Here, except for a common multiplication by either $1/\rho_1$ or $1/\rho_2$, the third term on the right-hand side is the negative reciprocal of the second term for both A_- and B. From the conventional von Neumann stability criterion in equation 21 (which I am assuming to be true; otherwise, instabilities would arise away from the interface), either $c_1^2\Delta t^2/h^2$ or $c_2^2\Delta t^2/h^2$ is at most equal to 1/3. Thus, the magnitude of the second term on the right-hand side is at least $4^2 \times 3^2 = 144$ times larger than the third term. Therefore, the third term can be safely ignored and I can and continue with

$$A_- \approx \frac{1}{2}\left(\frac{3}{\rho_1}+\frac{1}{\rho_2}\right) - \frac{4h^2}{\kappa_1\Delta t^2},$$
$$B \approx \frac{1}{2}\left(\frac{1}{\rho_1}+\frac{3}{\rho_2}\right) - \frac{4h^2}{\kappa_2\Delta t^2}. \quad (44)$$

Inserting these approximations for A_- and B into the exact stability criterion in equation 40 gives

$$\frac{1}{4}\left(\frac{1}{\rho_1}+\frac{1}{\rho_2}\right)^2 - A_-B \le 0. \quad (45)$$

Some algebraic manipulation gives an inequality that is quadratic in $h^2/\Delta t^2$:

$$\frac{16}{\kappa_1\kappa_2}\left(\frac{h}{\Delta t}\right)^4 - 2\left[\frac{1}{\rho_1\kappa_1}+\frac{3}{\rho_2\kappa_1}+\frac{3}{\rho_1\kappa_2}+\frac{1}{\rho_2\kappa_2}\right]\left(\frac{h}{\Delta t}\right)^2 + \frac{1}{2}\left(\frac{1}{\rho_1^2}+\frac{4}{\rho_1\rho_2}+\frac{1}{\rho_2^2}\right) \ge 0. \quad (46)$$

Denoting the coefficients of the quadratic as

$$a = \frac{16}{\kappa_1\kappa_2},$$
$$b = -2\left[\frac{1}{\rho_1\kappa_1}+\frac{3}{\rho_2\kappa_1}+\frac{3}{\rho_1\kappa_2}+\frac{1}{\rho_2\kappa_2}\right],$$
$$c = \frac{1}{2}\left(\frac{1}{\rho_1^2}+\frac{4}{\rho_1\rho_2}+\frac{1}{\rho_2^2}\right), \quad (47)$$

I find that there are two real roots because the discriminant can be written as the sum of positive quantities:

$$b^2 - 4ac = 32\left[\frac{1}{\rho_1^2\kappa_2^2}+\frac{1}{\rho_2^2\kappa_1^2}\right] + 4\left[\frac{1}{\rho_1^2}+\frac{6}{\rho_1\rho_2}+\frac{1}{\rho_2^2}\right] \times \left[\frac{1}{\kappa_1}-\frac{1}{\kappa_2}\right]^2. \quad (48)$$

Note that the use of the symbol c here, representing one of the coefficients of the quadratic, should not be confused with the earlier use of c as the acoustic wave speed.

From the two real roots of the quadratic, there are two conditions for the inequality in equation 46 to hold:

$$\sqrt{\frac{-b-\sqrt{b^2-4ac}}{2a}}\Delta t \le h$$

and

$$\sqrt{\frac{-b+\sqrt{b^2-4ac}}{2a}}\Delta t \le h. \quad (49)$$

The more stringent of these two inequalities becomes the stability criterion. From equation 47, b is seen to be a negative quantity. Thus, the more stringent of the two inequalities is

$$\sqrt{\frac{-b+\sqrt{b^2-4ac}}{2a}}\Delta t \le h. \quad (50)$$

Equation 50 is the stability criterion for an interface. It maintains the concise form of the usual von Neumann stability criterion (equation 21). Although it is derived using approximations, it is shown in the next section that it predicts the crossover from stable to unstable numerical behavior quite well.

In the above derivation, I have considered the case of normal incidence. In three dimensions, instabilities typically arise at spatial Nyquist frequencies, k_xh and $k_yh = \pi$, rather than k_x and $k_y = 0$. The analysis for this case mirrors the derivation just presented for normal incidence. I find another approximate stability criterion in this case that is identical in form to equation 50, except coefficients a, b, and c are given by

$$a = \frac{16}{\kappa_1\kappa_2},$$
$$b = -2\left[\frac{1}{\rho_1\kappa_1}+\frac{19}{\rho_2\kappa_1}+\frac{19}{\rho_1\kappa_2}+\frac{1}{\rho_2\kappa_2}\right],$$
$$c = \frac{9}{2}\left(\frac{1}{\rho_1^2}+\frac{18}{\rho_1\rho_2}+\frac{1}{\rho_2^2}\right). \quad (51)$$

I compare the stability criterion for the normal incidence case to the case of k_xh and $k_yh = \pi$ in Figure 7. For Figure 7, I define a quantity called the stability value, which is the left-hand side of equation 50 divided by the grid spacing h. Thus, the stability value S is given by

$$S = \sqrt{\frac{-b+\sqrt{b^2-4ac}}{2a}}\frac{\Delta t}{h}. \quad (52)$$

When the stability value exceeds unity, the resulting code becomes numerically unstable.

The model parameters used in Figure 7 are given in Table 1, except that the density in medium 2 (the transmitting medium) is allowed to vary from 2200 to 0 kg/m^2. It is evident in the plot that, as the density of medium 2 becomes smaller and smaller, the stability criterion for the case of k_xh and $k_yh = \pi$ is violated and exceeds unity prior to the normal incidence case. This points to the fact that instabilities arise in 3D numerical simulations as a result of waves with horizontal wavenumbers at the spatial Nyquist frequency, k_xh and $k_yh = \pi$.

I continue to investigate the interface stability criterion for the case of normal incidence (equation 50) by comparing the stability properties of an interface with a pure density contrast to that with a pure velocity contrast, as shown in Figure 8. The plot for a pure density contrast is identical to the one for normal incidence shown in

Figure 7. For the pure velocity contrast, I use the model parameters shown in Table 1, except that I set the density in medium 2 to the density in medium 1 and then let the velocity in medium 2 vary from 2500 to 0 m/s. The two panels in Figure 8 show these two cases. From these two plots, it can be seen that strong velocity contrasts and strong density contrasts have a markedly different effect on numerical stability. For a pure velocity contrast, as the velocity in medium 2 becomes smaller, the stability value never exceeds unity and actually decreases. In contrast, the pure density contrast goes unstable for small values of density in medium 2. This agrees with the observation that instabilities arise at strong density contrasts when using the standard staggered grid (Bartel et al., 2000; Saenger et al., 2000).

NUMERICAL VERIFICATION

To test these arguments, I utilize the interface stability criterion (equation 50) for the case of normal incidence when the coefficients a, b, and c are given by equation 47. After considering this case, I return to the example shown in the introduction and test the general 3D criterion given by equation 50, in which case a, b, and c are given by equation 51. I utilize a 3D acoustic finite-difference code developed within the Geophysics Department at Sandia National Laboratories; the code implements equations 7–10. To address stability for the normal-incidence case, I have equipped the 3D code with periodic boundary conditions and initiate a vertically propagating plane wave by setting off identical explosion sources over all gridpoints for a single depth slice of the model (at 2250-m depth). The identical explosion sources create outgoing plane waves with a wavelet whose dominant frequency is 10 Hz. Such a numerical setup has been applied to study the propagation of plane waves in microtomographic models using the finite-difference method (Saenger et al., 2004; Haney et al., 2006). The model I use is two half-spaces with a horizontal interface at 1500 m depth.

For the test, normal-incidence, acoustic plane waves are simulated in models 4 and 5. These models are described in Table 1. They differ only in that the density of the transmitting medium is 50 kg/m^3 for model 5 and 60 kg/m^3 for model 4. In Figure 8, the stability value for an interface with a pure density contrast exceeds unity and thus becomes numerically unstable for densities below roughly 52.5 kg/m^3. Therefore, models 4 and 5 straddle the predicted stability limit and should indicate whether the stability criterion (equation 50) is correct.

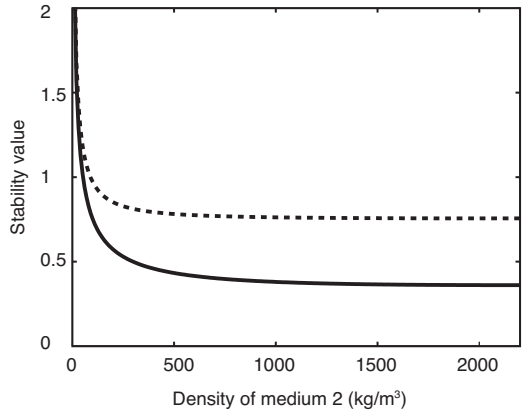

Figure 7. A comparison of numerical stability of a model with a pure density contrast for normal incidence $k_x = k_y = 0$ (solid line) and $k_x h = k_y h = \pi$ (dashed line). The stability value is plotted here as defined in equation 52. When the stability value exceeds unity, the simulation is unstable. The model parameters are given in Table 1, except that the density in medium 2 (the transmitting medium) varies continuously in the plot from 2200 to 0 kg/m^3. The stability criterion for the case of $k_x h = k_y h = \pi$ is more stringent than normal incidence and thus governs the onset of instabilities for general 3D acoustic-wave propagation.

Figure 9 shows the result of the test. As expected, the simulation for model 5 is disrupted by a strong numerical instability originating at the interface at 1500 m depth. This instability continues to increase rapidly in amplitude with each time step and eventually causes floating-point overflow. As also expected, the simulation for model 4 executes stably without an interface instability. It is worth noting that the plots of the wavefields in Figure 9e and f are after roughly 1280 time steps of the numerical algorithm. The simulation for model 4 continued to execute in a stable fashion until the simulation ended after 8000 time steps.

Finally, I return to the example shown in the introduction. This example used truly 3D wave propagation, so it provides a test of the general 3D stability criterion — equation 50 with coefficients a, b, and c given by equation 51. As shown in Figure 7, the crossover value of density for the general 3D case (determined by the behavior of the $k_x h = k_y h = \pi$ component) is given by approximately 89.5 kg/m^3. Note that this crossover value is higher than for the normal-incidence case. The two examples shown in Figure 2 are for model 2 (stable) and model 3 (unstable). From Table 1, it can be seen

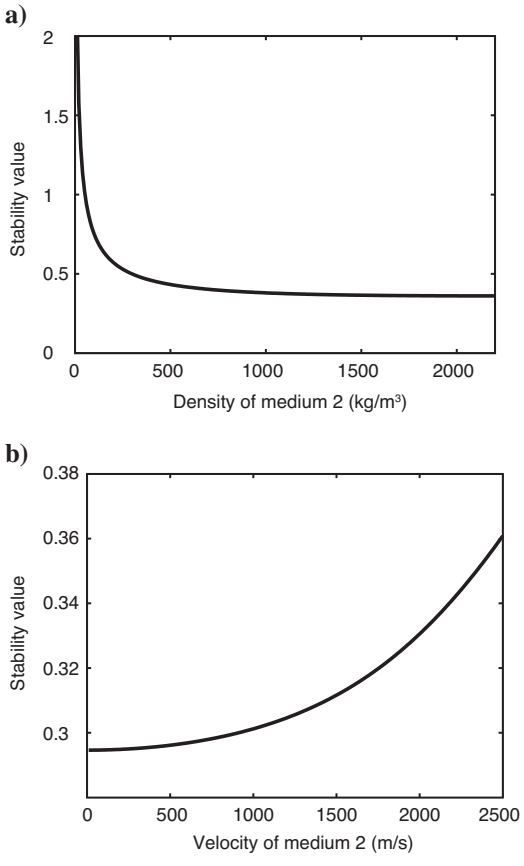

Figure 8. Comparison of the stability value, as defined in equation 52, for (a) an interface with a pure density contrast and (b) a pure velocity contrast in the case of normal incidence. The density contrast at an interface is the controlling factor in generating instabilities.

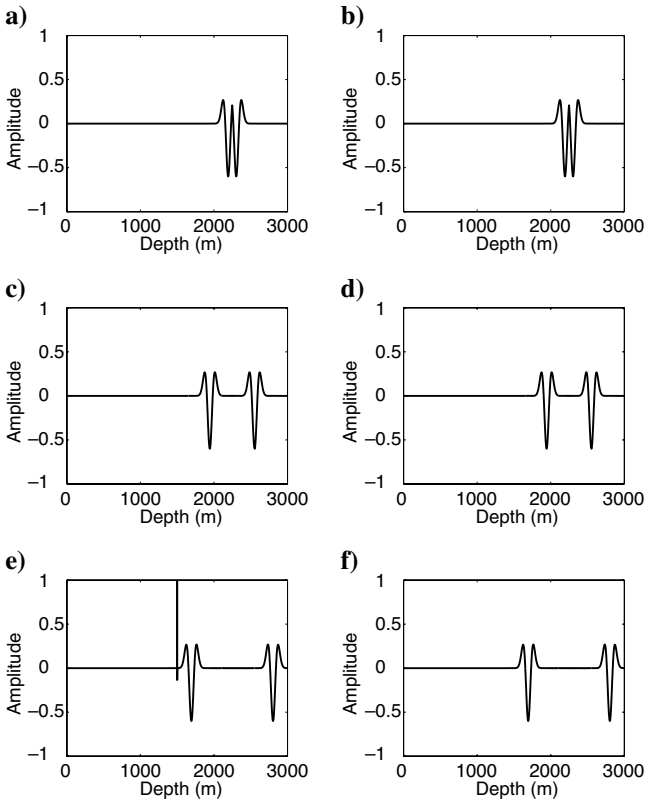

Figure 9. Test of the interface stability criterion using a 3D acoustic finite-difference code. The pressure wavefield is shown at three different times along a vertical line through a model with an interface at 1500-m depth. A planar explosion source is initiated at 2250-m depth. The times shown are (a, b) 0.02 s, (c, d) 0.12 s, and (e, f) 0.22 s after source initiation. Panels (a), (c), and (e) show a simulation using model 5, and panels (b), (d), and (f) show a simulation for model 4. These two models are the same except that model 5 has a slightly greater density contrast across the interface. This causes an instability to develop at the interface in (e) for model 5, in contrast to the simulation for model 4. The difference in stability for these two models is in agreement with the stability condition developed using a generalized von Neumann analysis.

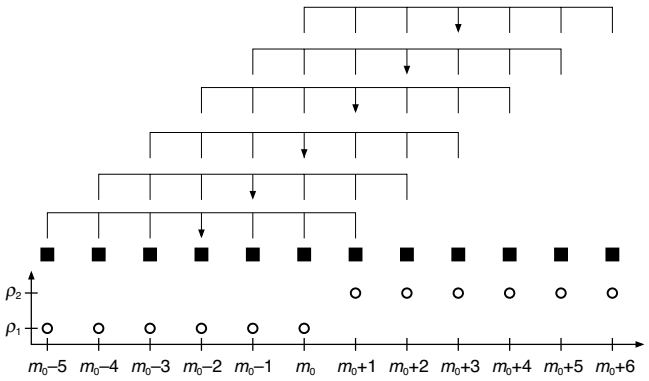

Figure 10. A fourth-order scheme in space. There are six wave modes in this case (three upgoing and three downgoing waves); thus, six relationships are needed to solve for the three reflected and three transmitted waves from the discrete interface. These six relationships are given by the six instances where a fourth-order finite-difference stencil overlaps between the two half-spaces.

that these two models indeed straddle the crossover value of density: Model 2 has a density of 100 kg/m^3 for medium 2, and model 3 has a density of 80 kg/m^3 for medium 2. The numerical stability of the examples in the introduction are well predicted by the new stability criterion I derive for the general 3D case. Thus, the stability criteria for both the normal incidence and general 3D cases have been independently verified by executing a 3D finite-difference code.

EXTENSION TO NUMERICAL SCHEMES WITH HIGHER-ORDER SPATIAL ACCURACY

I have described how to derive a highly accurate stability condition for interface instabilities in an $O(2,2)$ scheme. How does this generalize to a schemes with higher-order spatial accuracy? Here I illustrate the case of $O(2,4)$, a popular finite-difference scheme (Graves, 1996; Moczo et al., 2000). For an $O(2,4)$ scheme, six different wave types exist: three upgoing and three downgoing waves. This is because the analogy of equation 22 for an $O(2,4)$ scheme is cubic instead of linear in the quantity $\cos k_z h$. Four of the six wave types in this case are known as computational modes (Haltiner and Williams, 1980; p. 114) or parasitic modes (Marfurt, 1984; p. 541). These four wave types do not survive in the continuum limit. Nevertheless, away from the continuum limit, they do exist and must be taken into account when solving for discrete reflection and transmission coefficients at an interface.

Since all six wave types must be considered in solving for the discrete reflection and transmission coefficients, there are six unknown for a given incident wave type. These six unknowns are the three reflection and three transmission coefficients. To calculate all six of these coefficients, six equations relating the wavefields in the two half-spaces are needed. It turns out that, analogous to equation 29, the stencil for pressure at vertical index m, P_m, in the $O(2,4)$ scheme depends on the six nearest gridpoints: P_{m-3}, P_{m-2}, P_{m-1}, P_{m+1}, P_{m+2}, and P_{m+3}. As shown in Figure 10, this stencil has exactly six positions where it overlaps between the two half-spaces. These six positions lead to the six equations necessary to solve for the discrete reflection and transmission coefficients. Although the methodology outlined in this paper is perfectly applicable to the $O(2,4)$ case, the algebraic complexity of performing the process increases dramatically.

CONCLUSIONS

With the aim of generalizing von Neumann analysis to allow for medium heterogeneity, I have successfully created an extension of the technique for the simplest kind of heterogeneous model — one consisting of two half-spaces. In pursuit of a stability condition for interface instabilities, I began by obtaining closed-form solutions for numerical reflection and transmission coefficients. The ability to compute these coefficients means comparisons of various finite-difference schemes are not limited to discussions of dispersion and stability for a homogeneous whole space. The quantitative comparison of different algorithms may also address the accuracy of reflection and transmission at a discrete interface. Using the expressions for numerical reflection and transmission coefficients, I found that instabilities at interfaces with strong material contrasts occur because the reflection and transmission coefficients become unbounded for exponentially growing solutions. I then developed approximate stability conditions so these interface instabilities may be understood and parameters chosen such that they do not occur. Although approximate, a numerical test showed that the stability condition pre-

dicts the crossover from unstable to stable numerical behavior quite accurately. The stability criterion should find application alongside the conventional von Neumann stability condition for avoiding instabilities in acoustic models with strong density contrasts across interfaces. The density contrasts required to cause these instabilities are large, but such contrasts could exist in realistic models at the air-earth or air-ocean interface, for models of the subsurface containing open subterranean structures or caverns, and in pore-scale numerical modeling when air or vacuum is placed in the pore space.

Future applications of generalized von Neumann analysis include an investigation of reflection and transmission from models with spatially variable grid spacings, reflection and transmission from interfaces that are not aligned with the finite-difference grid, and performance of numerical schemes besides the standard staggered grid, such as the rotated staggered grid. An extension to the elastic case is also planned. The elastic situation will be complicated by the fact that surface waves at an interface (Rayleigh or Stoneley waves) have the property of satisfying the interface boundary conditions without the need for an incident wave. This property plays an important role in generating numerical instabilities at an interface as well.

ACKNOWLEDGMENTS

The author is grateful to David Aldridge of Sandia National Laboratories for interesting discussions and assistance in understanding von Neumann analysis. Additional thanks are given to the weekly seminar group at the Center for Wave Phenomena, Colorado School of Mines (CSM), for providing feedback on an early version of this work and, in particular, Dave Hale. John Scales of CSM provided a copy of the Fermi, Pasta, and Ulam paper. Sandia National Laboratories is a multiprogram science and engineering facility operated by Sandia Corporation, a Lockheed-Martin Company, for the U. S. Department of Energy under contract DE-AC04-94AL85000. The author acknowledges partial funding from the U. S. Department of Energy, Office of Basic Energy Sciences, Chemical Sciences and Geosciences Program.

REFERENCES

Aldridge, D. F., L. C. Bartel, and N. P. Symons, 2004, Velocity-stress-pressure algorithm for 3D poroelastic wave propagation: 74th Annual International Meeting, SEG, Expanded Abstracts, 1917–1920.

Alterman, Z. S., and D. Loewenthal, 1970, Seismic waves in a quarter and three-quarter plane: Geophysical Journal of the Royal Astronomical Society, **20**, 101–126.

Bartel, L. C., N. P. Symons, and D. F. Aldridge, 2000, Graded boundary simulation of air/earth interfaces in finite-difference elastic wave modeling: 70th Annual International Meeting, SEG, Expanded Abstracts, 2444–2447.

Bednar, J. B., W. L. Abriel, B. Biondi, S. Levin, and A. Cheng, 2006, SEG advanced modeling (SEAM) today and tomorrow: 76th Annual International Meeting, SEG, Expanded Abstracts, 3531–3534.

Claerbout, J. F., 1976, Fundamentals of geophysical data processing: Blackwell Scientific Publications.

Cohen, G. C., 2001, Higher order numerical methods for transient wave equations: Springer-Verlag New York, Inc.

Crase, E., 1990, High-order (space and time) finite-difference modeling of the elastic wave equation: 60th Annual International Meeting, SEG, Expanded Abstracts, 987–991.

Fermi, E., J. Pasta, and S. Ulam, 1955, Studies of nonlinear problems: Los Alamos Scientific Laboratory Technical Document LA-1940.

Graves, R. W., 1996, Simulating seismic wave propagation in 3D elastic media using staggered-grid finite differences: Bulletin of the Seismological Society of America, **86**, 1091–1106.

Haltiner, G. J., and R. T. Williams, 1980, Numerical prediction and dynamic meteorology: John Wiley & Sons, Inc.

Haney, M. M., J. T. Fredrich, B. J. Zadler, J. A. Scales, and D. F. Aldridge, 2006, Numerical simulation of resonances in microtomographic models: 76th Annual International Meeting, SEG, Expanded Abstracts, 1841–1844.

Hestholm, S., 2003, Elastic wave modeling with free surfaces: Stability of long simulations: Geophysics, **68**, 314–321.

Kelly, K. R., and K. J. Marfurt, eds., 1990, Numerical modeling of seismic wave propagation: Geophysics Reprint Series 13, SEG.

Kelly, K. R., R. W. Ward, S. Treitel, and R. M. Alford, 1976, Synthetic seismograms: A finite-difference approach: Geophysics, **41**, 2–27.

Komatitsch, D., and J. Tromp, 1999, Introduction to the spectral-element method for three-dimensional seismic wave propagation: Geophysical Journal International, **139**, 806–822.

Koteras, J. R., and R. B. Lehoucq, 2007, Estimating the critical time-step in explicit dynamics using the Lanczos method: International Journal for Numerical Methods in Engineering, **69**, 2780–2788.

Lay, T., and T. C. Wallace, 1995, Modern global seismology: Academic Press Inc.

Levander, A. R., 1988, Fourth-order finite-difference P-SV seismograms: Geophysics, **53**, 1425–1436.

Lines, L. R., R. Slawinski, and R. P. Bording, 1999, A recipe for stability of finite-difference wave-equation computations: Geophysics, **64**, 967–969.

Marfurt, K. J., 1984, Accuracy of finite-difference and finite-element modeling of the scalar and elastic wave equations: Geophysics, **49**, 533–549.

Moczo, P., J. Kristek, and L. Halada, 2000, 3D fourth-order staggered-grid finite-difference schemes: Stability and grid dispersion: Bulletin of the Seismological Society of America, **90**, 587–603.

———, 2004, The finite-difference method for seismologists: An introduction: Comenius University Press.

Moczo, P., J. Kristek, V. Vavryčuk, R. J. Archuleta, and L. Halada, 2002, 3D heterogeneous staggered-grid finite-difference modeling of seismic motion with volume harmonic and arithmetic averaging of elastic moduli and densities: Bulletin of the Seismological Society of America, **92**, 3042–3066.

Oppenheim, A. V., and A. S. Willsky, 1983, Signals and systems: Prentice-Hall, Inc.

Press, W. H., S. A. Teukolsky, W. T. Vetterling, and B. P. Flannery, 1986, Numerical recipes in FORTRAN: The art of scientific computing: Cambridge University Press.

Saenger, E. H., N. Gold, and S. A. Shapiro, 2000, Modeling the propagation of elastic waves using a modified finite-difference grid: Wave Motion, **31**, 77–92.

Saenger, E. H., O. S. Krüger, and S. A. Shapiro, 2004, Numerical considerations of fluid effects on wave propagation: Influence of the tortuosity: Geophysical Research Letters, **31**, L21613.

Scales, J. A., 1995, Theory of seismic imaging, Springer-Verlag Berlin.

Seron, F. J., J. Badal, and F. J. Sabadell, 1996, A numerical laboratory for simulation and visualization of seismic wavefields: Geophysical Prospecting, **44**, 603–642.

Tsvankin, I., 1995, Seismic wavefields in layered isotropic media: Samizdat Press, accessed April 27, 2007 ⟨http://samizdat.mines.edu/waves_layered_media/⟩.

Virieux, J., 1984, SH wave propagation in heterogeneous media: Velocity-stress finite-difference method: Geophysics, **49**, 1933–1957.

———, 1986, P-SV wave propagation in heterogeneous media: Velocity-stress finite-difference method: Geophysics, **51**, 889–901.

Wapenaar, C. P. A., J. L. T. Grimbergen, and F. J. Dessing, 1995, One-way operators in laterally varying media: 65th Annual International Meeting, SEG, Expanded Abstracts, 1141–1144.

Zahradník, J., and E. Priolo, 1995, Heterogeneous formulations of elastodynamic equations and finite-difference schemes: Geophysical Journal International, **120**, 663–676.